nanomaterials

MDPI

Article

Combined Spectroscopic and Computational Study of Nitrobenzene Activation on Non-Noble Metals-Based Mono- and Bimetallic Catalysts

Reisel Millán, María Dolores Soriano, Cristina Cerdá Moreno, Mercedes Boronat * and Patricia Concepción *

Instituto de Tecnología Química (UPV-CSIC), Universitat Politècnica de València—Consejo Superior de Investigaciones Científicas, Avda. de los Naranjos s/n, 46022 Valencia, Spain; reimilca@itq.upv.es (R.M.); mdosorod@itq.upv.es (M.D.S.); cricermo@itq.upv.es (C.C.M.)

* Correspondence: boronat@itq.upv.es (M.B.); pconcepc@upvnet.upv.es (P.C.)

Abstract: In this paper, substituted anilines are industrially obtained by direct hydrogenation of nitroaromatic compounds with molecular H_2 using metals as catalysts. Previous theoretical studies proposed that the mechanism of the reaction depends on the nature of the metal used as a catalyst, and that rationally designed bimetallic materials might show improved catalytic performance. Herein, we present IR spectroscopic studies of nitrobenzene interactions with monometallic Ni/SiO_2, Cu/SiO_2 and Pd/SiO_2, and with bimetallic $CuNi/SiO_2$ and $CuPd/SiO_2$ catalysts, both in the absence and presence of H_2, combined with density functional theory (DFT) calculations on selected bimetallic NiCu(111) and PdCu(111) models. The results obtained experimentally confirm that the reaction mechanism on non-noble metals such as Ni proceeds through N-O bond dissociation, generating nitrosobenzene intermediates, while, on noble metals, such as Pd, H-attack is necessary to activate the NO bond. Moreover, a bimetallic $CuPd/SiO_2$ catalyst with a Pd enriched surface is prepared that exhibits an enhanced H_2 dissociation ability and a particular reactivity at the boundary between the two metals.

Keywords: nitrobenzene hydrogenation; IR spectroscopy; DFT; bimetallic catalysts; non-noble metals

Citation: Millán, R.; Soriano, M.D.; Cerdá Moreno, C.; Boronat, M.; Concepción, P. Combined Spectroscopic and Computational Study of Nitrobenzene Activation on Non-Noble Metals-Based Mono- and Bimetallic Catalysts. *Nanomaterials* **2021**, *11*, 2037. https://doi.org/10.3390/nano11082037

Academic Editor: Junying Zhang

Received: 22 July 2021
Accepted: 6 August 2021
Published: 10 August 2021

1. Introduction

Aniline and its derivatives are widely used in the chemical industry to produce a diversity of pharmaceuticals, agrochemicals, polymers and dyes [1,2]. Aniline is industrially obtained by direct nitrobenzene hydrogenation with H_2 using Ni-Raney or noble metal-based heterogeneous catalysts. However, the chemoselective hydrogenation of the nitro group in substituted nitroaromatic compounds containing C=C, C=O, C≡N or halogens, which must remain unaffected during the reaction, is more challenging and requires the use of modifiers, dopants or promoters [3–8]. Alternatively, noble metal nanoparticles of Au, Ag or Pt, supported on metal oxides such as TiO_2, Al_2O_3 or FeO_x [9–12], Pt atomically dispersed over α-MoC [13], Pt particles or nanocrystals partly covered by TiO_2 or $Fe(OH)_x$ [14–16], Pd and Pt nanoparticles dispersed on carbon or capped with organic ligands [17,18], are highly chemoselective hydrogenation catalysts. The origin of this chemoselectivity usually relies on the preferential adsorption of the nitroaromatic reactant through the nitro group, so that the other functional groups remain unreachable for hydrogenation [19–21].

The high cost of noble metals has led to an important research effort to develop catalysts based on cheaper and more abundant non-noble metals [8]. In recent years, promising results have been reported with Co_3O_4 and Fe_2O_3 nanoparticles stabilized on carbon and N-doped carbon supports [22–24], as well as with mono- [25–30] and bimetallic [31–36] catalysts containing either atomically dispersed species or nanoparticles of Ni, Co, Cu, Fe or combinations of them, supported, in most cases, on carbon-containing materials. In

contrast with the large number of publications reporting catalytic data, little attention has been paid to the reaction mechanism at the molecular level, and the macroscopic scheme proposed by Haber in 1898 [37] is still used to rationalize the catalytic results. According to Haber's mechanism (Scheme 1a), there are two main pathways to reduce the nitro group in nitrobenzene: (i) the direct route comprises three successive hydrogenation steps that convert nitrobenzene into nitrosobenzene, phenyl-hydroxylamine and, finally, aniline; (ii) in the condensation route, nitrosobenzene and phenyl-hydroxylamine intermediates react to form an azoxy compound that is transformed, by successive hydrogenation steps, into azo and hydrazo intermediates and, finally, the aniline product. Some computational studies of the reaction mechanism on noble metal [17,38,39] and non-noble metal surfaces [40–42] indicate that different pathways are followed on each type of catalyst (see Scheme 1b). On noble metals, such as Pt or Pd, the dissociation of the NO bonds is difficult and requires their previous transformation into weaker N–OH bonds through H attack, leading to the formation of hydroxylamine intermediates. In contrast, on non-noble metals, such as Ni or Co, the high oxophylicity of the metal surface facilitates NO bond breaking, and the reaction involves fast formation of nitrosobenzene intermediates. While this proposal is indirectly supported by analysis of the product distribution on Ni@C catalysts [41], a detailed and systematic characterization of the most relevant reaction intermediates on comparable noble and non-noble metal catalysts is still missing; this is the first motivation of the present work. In addition, a comparison of the energy profiles obtained from DFT simulations on Ni, Co, Cu and Pd surfaces showed that Cu is somewhat different from the other non-noble metals [42]. On one hand, aromatic rings do not interact strongly with the Cu(111) face; therefore, nitroaromatic compounds always adsorb in a normal orientation with respect to the metal surface, leading to a high intrinsic chemoselectivity in the case of substituted nitroaromatics. On the other hand, the activation energy barriers for the most difficult hydrogenation steps are lower on Cu(111) than in other non-noble metals, suggesting that alloying Cu with another metal able to activate H_2 efficiently could result in a highly active and fully chemoselective catalyst [42].

In this work, monometallic Ni/SiO_2, Cu/SiO_2 and Pd/SiO_2, and bimetallic $CuNi/SiO_2$ and $CuPd/SiO_2$ catalysts, have been prepared in the form of large metal nanoparticles on an inert support. IR studies of nitrobenzene adsorption in the absence and presence of H_2 have been conducted to identify the key reaction intermediates, and the results have been rationalized with the assistance of DFT simulations. Our study operates from a fundamental point of view rather than catalytic one, unravelling the different reaction mechanisms on noble and non-noble metal catalysts.

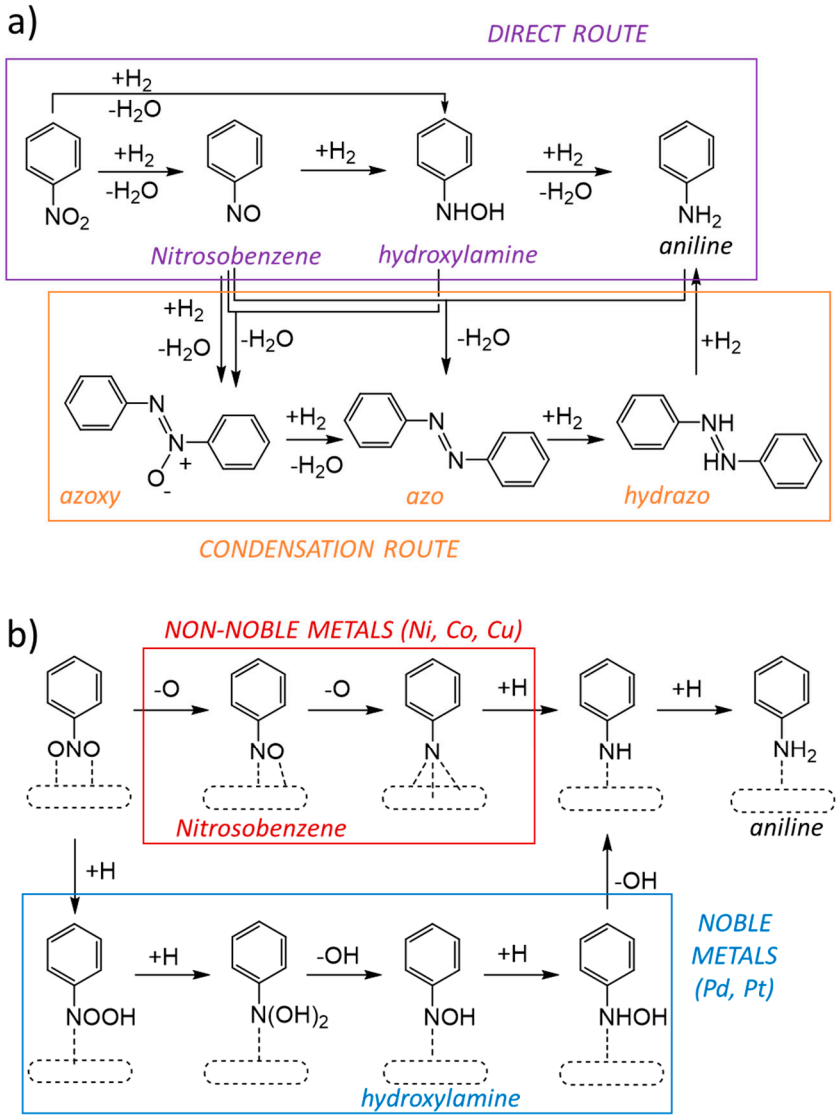

Scheme 1. (**a**) Direct (purple) and condensation (orange) routes of the mechanism proposed by Haber for hydrogenation of nitrobenzene. (**b**) Possible pathways for the direct route of the mechanism on non-noble metals (red) and noble metals (blue).

2. Materials and Methods

2.1. Catalyst Synthesis and Characterization

2.1.1. Catalyst Synthesis

Supported catalysts were synthesized by dissolving the corresponding amounts of nickel (II) nitrate hexahydrate, copper (II) nitrate trihydrate or palladium (II) hydrate (Sigma-Aldrich, St. Louis, MO, USA) in deionized water. Amorphous silica (200 m^2/g) was added to this solution and was evaporated, dried overnight at 120 °C and, finally, calcined in static air at 500 °C for 2 h. Then, the solid obtained was reduced in H_2 flow at 350 °C for 2 h. For example, in the case of monometallic samples, i.e., Ni/SiO_2, 2.5 g of nickel (II) nitrate hexahydrate was dissolved in 40 mL of water. Then, 1.5 g of amorphous silica was added to this solution and evaporated. A green solid was obtained, which was calcined and reduced. Similar procedures have been used for the Cu/SiO_2 and Pd/SiO_2 samples. In the bimetallic samples, i.e., $Cu_{0.5}Pd/SiO_2$, 1.9 g of copper (II) nitrate trihydrate and 0.03 g of palladium (II) hydrate was dissolved in 40 mL of water. Then, 1.5 g of amorphous silica was added to this solution and evaporated. Similar procedures have been used for

the Cu_2Pd/SiO_2 and Cu_2Ni/SiO_2, but the amount of palladium (II) hydrate (0.09 g) or nickel (II) nitrate hexahydrate (0.2 g), respectively, was modified.

2.1.2. Characterization

The metal content was analyzed by inductively coupled plasma optical emission spectrometry (ICP-OES) using a Varian 715-ES spectrometer.

Powder X-ray diffraction patterns (XRD) were recorded with a Philips XPert diffractometer using monochromatic Cu Kα radiation (λ = 0.15406 nm). Average particle size was calculated from the main peaks using the Scherrer equation. XRD of reduced samples was performed immediately after the ex situ reduction while expositing to air for analysis.

Temperature programmed reduction (TPR) was performed using a micromeritics Autochem 2910 apparatus with a TCD detector. The reducing gas used was 10% H_2 in argon, with a total flow rate of 50 mL·min^{-1} (GHSV ca. 8000 h^{-1}). The temperature range explored was from room temperature to 400 °C, with a heating rate of 10 °C·min^{-1}.

X-ray photoelectron spectroscopy (XPS) measurements were performed on a SPECS spectrometer equipped with a Phoibos 150 MCD-9 detector using non-monochromatic Al Kα (1486.6 eV) X-ray radiation. The pass energy was 30 eV and the X-ray power was 100 W. Spectra treatment was performed using CASA software. Binding energies (BE) were referenced to C1s at 284.5 eV.

Hydrogen/deuterium (H_2/D_2) exchange experiments were carried out in a flow reactor at 25 °C. The feed gas consisted of 4 mL·min^{-1} H_2, 4 mL·min^{-1} D_2 and 18 mL·min^{-1} argon, and the total weight of the catalyst was 10 mg. The sample was diluted with 390 mg of SiC. Reaction products (H_2, HD and D_2) were analyzed with a mass spectrometer (Omnistar, Balzers). The m/z values used were 2 (H_2), 4 (D_2) and 3 (HD). The sample was in situ reduced at 240 °C (28 mL·min^{-1}; 35.7 vol % H_2) for 90 min with a temperature-rising rate of 10 °C·min^{-1}. Then, the temperature was decreased to 25 °C and, once stabilized, the H_2 feed was changed to the reactant gas composition. The temperature was kept at 25 °C for about 60 min.

2.2. IR Spectroscopy

The nature of the surface metal species and their reactivity were assessed by FTIR spectroscopy. Infrared spectra were acquired on a Bruker Vertex 70 with a DTGS detector at a resolution of 4 cm^{-1}. Samples were pressed into self-supported wafers and introduced in a home-made IR cell, which was connected to both a system allowing in situ treatments and a vacuum system with a gas dosing facility.

First, samples were submitted to activation at 240 °C in H_2 flow (10 mL·min^{-1}) for 1.5 h and then evacuated under dynamic vacuum of 10^{-5} mbar at 290 °C for 1 h. Next, the temperature in the cell was decreased to room temperature prior to reactants dosing. Samples were studied in terms of nitrobenzene adsorption and its reactivity with H_2. In the first case, nitrobenzene was dosed at room temperature until saturation (~0.3 mbar, i.e., 3.68×10^{-6} mol) while, in the second one, after nitrobenzene adsorption at room temperature, samples were evacuated; then, H_2 (~12 mbar, i.e., 147×10^{-6} mol) was introduced to the cell. After nitrobenzene or nitrobenzene/H_2 dosing, the temperature of the cell was increased to 60, 90, 120, 140, 160, 180 and 200 °C, and the evolution of the formed species followed at each temperature, acquiring the IR spectrum after 20 min.

For the CO titration experiments, CO was used as probe molecule to characterize the surface species of the catalyst. In this case, after sample pre-activation under similar conditions as before, the temperature of the sample was decreased to −170 °C under dynamic vacuum conditions (10^{-5} mbar). At that temperature, CO was introduced to the cell at increasing pressures from 0.1 to 9 mbar. An IR spectrum was recorded after each dose.

2.3. Computational Details

Periodic density functional theory (DFT) calculations were performed with the VASP code [43] using the GGA-type functional of Perdew, Burke and Ernzerhof (PBE) [44,45] and the Grimme D3 method to take into account dispersion interactions [46]. The valence density was expanded in a plane wave basis set with a kinetic energy cutoff of 450 eV, and the effect of the core electrons in the valence density was taken into account by means of a projected augmented wave (PAW) formalism [47,48]. All calculations were spin polarized. Electronic energies were converged to 10^{-6} eV and geometries were optimized by means of a conjugate gradient algorithm, until forces on atoms were smaller than 0.01 eV/Å. Transition state structures were located using the DIMER algorithm [49,50], and vibrational frequencies were calculated numerically.

The catalyst surface was simulated by means of a supercell slab model consisting of five atomic layers oriented along the (111) plane, which is the most stable and preferentially exposed in the metal catalysts considered here, and separated by a vacuum region of 10 Å to avoid interaction between periodically repeated slabs. The size of the supercell slab was also large enough to avoid interaction between the periodically repeated adsorbates.

H_2 dissociation was investigated using a (3 × 3) supercell slab containing 45 metal atoms as catalyst model, and integration in the reciprocal space was carried out using a converged Monkhorst-Pack mesh of 6 × 6 × 1 k-points [51]. Nitrobenzene adsorption and hydrogenation were investigated using a larger 4 × 6 supercell slab containing 120 metal atoms, and integration in the reciprocal space was carried out at the Γ k-point of the Brillouin zone. During the geometry optimizations, the atomic positions of the adsorbates and the metal atoms in the two uppermost layers were allowed to fully relax, while the metal atoms in the three bottom layers were kept fixed at their bulk optimized positions. For each system, adsorption (E_{ads}), activation (E_{act}) and reaction (ΔE) energies were calculated as:

$$E_{ads} = E(\text{slab-adsorbate}) - E(\text{slab}) - E(\text{adsorbate}) \quad (1)$$

$$Eact = E(TS) - E(R) \quad (2)$$

$$\Delta E = E(P) - E(R) \quad (3)$$

where E(slab-adsorbate), E(slab) and E(adsorbate) are the total energies of the optimized M(111)-adsorbate complex, clean M(111) surface model and isolated adsorbate molecule, respectively. For each elementary step considered, E(R), E(TS) and E(P) are the total energies of the corresponding reactant complex, transition state and product, respectively. Vibrational frequencies were calculated by diagonalizing the block Hessian matrix corresponding to displacements of the adsorbates. Absolute Gibbs free energies of all species were calculated as:

$$G = E_{tot} + E_{zpe} + E_{vib} - TS_{vib} \quad (4)$$

where E_{tot} is the electronic energy obtained from the DFT calculation, E_{zpe} is the zero-point energy correction, E_{vib} is the vibrational thermal energy contribution and S_{vib} is the vibrational entropy. The vibrational contributions to the energy and entropy were calculated according to:

$$E_{zpe} = \sum_{i=1}^{3N-6} \frac{1}{2} h\upsilon_i \quad (5)$$

$$E_{vib} = R \sum_{i=1}^{3N-6} \frac{h\upsilon_i}{k_B\left(e^{h\upsilon_i/k_BT} - 1\right)} \quad (6)$$

$$S_{vib} = R \sum_{i=1}^{3N-6} \left[\frac{h\upsilon_i}{k_BT\left(e^{h\upsilon_i/k_BT} - 1\right)} - \ln\left(1 - e^{h\upsilon_i/k_BT}\right) \right] \quad (7)$$

using the vibrational frequencies ν obtained from the DFT calculations.

3. Results

3.1. Synthesis and Characterization of Monometallic Ni/SiO_2, Cu/SiO_2 and Pd/SiO_2 Catalysts

In order to compare with the results from computational studies performed on extended (111) metal surface slab models, catalyst samples with high metal loadings, supported on SiO_2 as a low dispersive support, were prepared following the procedures described in the Materials and Methods section. The metal loading determined by ICP-AES is around 23 wt% in all samples (see Table 1). The XRD patterns of the monometallic catalysts are shown in Figure S1. In the case of the calcined materials, diffraction peaks corresponding to NiO (JCPDS: 78-643), CuO (JCPDS: 48-1548) and PdO (JCPDS: 6-515) are observed in the Ni/SiO_2, Cu/SiO_2 and Pd/SiO_2 samples, respectively (Figure S1a). On the other hand, the XRD patterns of the monometallic catalysts after reduction (Figure S1b) reveal the complete reduction of the metals showing diffraction peaks corresponding to Ni^0 (JCPDS: 4-850), Cu^0 (JCPDS: 4-836) and Pd^0 (JCPDS: 87-643). The average metal particle sizes in the reduced Ni/SiO_2, Cu/SiO_2 and Pd/SiO_2 samples, determined according to the Scherrer equation, are 20, 36, and 29 nm, respectively (Table 1).

Table 1. Physico-chemical properties of monometallic catalysts.

Sample	ICP (%)	H_2 [a] mmol/g	nm [b]	HD/H_2 [c]
Ni/SiO_2	23.0	n.d [d]	19.7	n.d.
Cu/SiO_2	24.0	5.39	35.9	0.058×10^{-1}
Pd/SiO_2	23.8	n.d.	28.7	n.d.

[a] H_2 consumptions in the TPR experiments undertaken until 400 °C. [b] Metal particle size determined by the XRD pattern of the reduced samples. [c] HD (mA) in the H_2D_2 isotopic exchange studies relative to the H_2 (mA) in the feed. [d] n.d. = not determined.

3.2. IR Study of Nitrobenzene Hydrogenation on Monometallic Ni/SiO_2, Cu/SiO_2 and Pd/SiO_2 Catalysts

With the aim of understanding the mechanism of nitrobenzene activation in the presence of non-noble metals such as Cu and Ni, compared to that of noble metals such as Pd, IR studies of nitrobenzene adsorption in the absence or presence of H_2 were conducted on the respective monometallic supported catalysts, and the results were compared with previous DFT studies performed by our group [41,42]. The adsorption of nitrobenzene on the monometallic catalysts results in several IR bands, where the peaks at 1531 and 1350 cm^{-1} correspond to the asymmetric and symmetric stretching vibration of the nitro group, respectively, and the band at 1480 cm^{-1} corresponds to the aromatic ring [52]. The position of those peaks appears at the same frequency independently of the type of metal Ni, Cu or Pd (Figure S2), revealing a similar adsorption configuration. However, while DFT studies suggest a flat adsorption mode of the aromatic ring of nitrobenzene and the Pd surface [42], which, based on the IR selection rules, would be inactive, this may not be the case in our study, probably due to the higher coverage of adsorbed molecules favoring, in all cases, a tilted interaction between the nitro group and the metal surface. Despite this similar initial configuration, a different behavior is observed at increasing temperature depending on the type of metal. In particular, on Cu/SiO_2 and Pd/SiO_2 catalysts, the IR bands at 1531 and 1480 cm^{-1} decrease in intensity at increasing temperature without the formation of new IR bands, reflecting a low surface interaction in both cases (Figure 1a,b). By contrast, on the Ni/SiO_2 catalyst, new IR bands are formed at an increasing reaction temperature concomitant with the decrease in intensity of the IR bands at 1531 and 1480 cm^{-1} (Figure 1c). Thus, at 60 and 90 °C, a shoulder at 1486 cm^{-1} is observed in the original 1480 cm^{-1} peak, which, at increasing temperature, grows in intensity, appearing as a unique peak at 180 °C. This band corresponds to nitrosobenzene [52,53], which is formed after N–O bond cleavage of the NO_2 group on the nickel surface, and remains stable even after increasing the temperature to 200 °C. DFT studies revealed a high tendency of N–O cleavage on Ni, supporting the IR data [41,42]. Once the nitrosobenzene has been formed on the Ni/SiO_2

catalyst, the co-addition of H_2 at 25 °C and further increasing the temperature results in aniline formation (IR band at 1605, 1500 and 694 cm^{-1}) [53] in a fast step, without the detection of intermediate species (Figure S3).

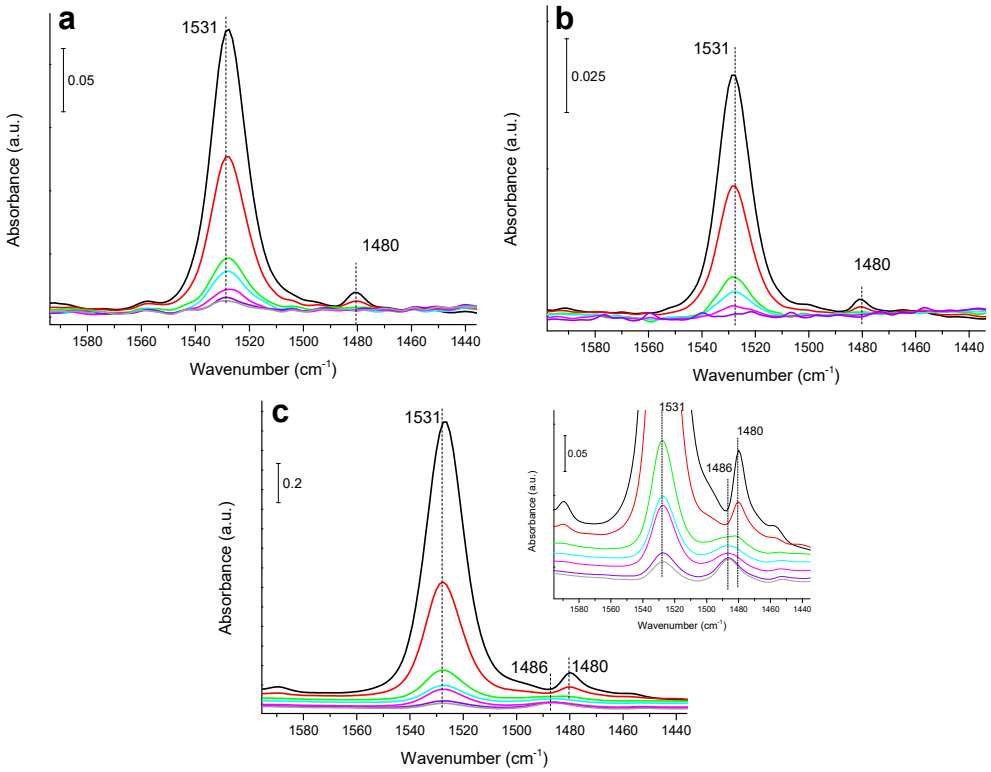

Figure 1. IR spectra of nitrobenzene adsorption on: (**a**) Cu/SiO_2, (**b**) Pd/SiO_2 and (**c**) Ni/SiO_2 (in the inset a zoom of the bottom part of the IR spectra), and their evolution with the temperature: 25 °C (black), 60 °C (red), 120 °C (green), 140 °C (cyan), 160 °C (magenta), 180 °C (violet) and 200 °C (grey).

In a second part of our work, the reactivity of surface-activated nitrobenzene in the presence of H_2 has been followed by IR studies. Different reaction trends are observed, from a very high reactivity on Pd/SiO_2 to an intermediate one on Ni/SiO_2, and a non-reactivity on Cu/SiO_2 catalysts (Figure 2). In particular, in the case of the Pd/SiO_2 catalyst (Figure 2a), aniline (IR bands at 1605 and 1500 cm^{-1}) is already formed at 25 °C in the presence of both nitrobenzene and H_2. The reactivity is almost complete, confirmed by the low intensity of the IR band of the asymmetric vibration of the nitro group at 1531 cm^{-1}. In the case of the Ni/SiO_2 catalyst (Figure 2b,c), nitrosobenzene (IR band at 1488 cm^{-1}) is formed at 60 °C and, at 90 °C, aniline (IR bands at 1604, 1500 and 694 cm^{-1}) starts to form. When increasing temperature from 90 to 200 °C, aniline and nitrosobenzene remain co-adsorbed, while nitrobenzene is completely transformed. Aniline is partially desorbed to the gas phase, as detected in the IR spectra after cooling down the sample (Figure S4). The conversion to the final product, i.e., aniline, is not complete, as it is in the case of the Pd/SiO_2 catalyst. DFT calculations performed by our group [41,42] indicate a progressive blocking of active sites in Nickel-based catalysts due to O* species resulting from N–O cleavage, which are not effectively removed by H_2. This may explain the lower formation of aniline in the Ni/SiO_2 versus Pd/SiO_2 catalyst. Unfortunately, the formation of Ni–O species under reaction conditions could not be detected by IR and Raman studies, being in the detection limit of both techniques. Finally, in the case of the Cu/SiO_2 catalyst (Figure 2d), nitrobenzene hydrogenation does not take place, due to its low reactivity toward H_2 dissociation. In fact, H_2D_2 isotopic experiments reveal a very low isotopic HD exchange in the case of the Cu/SiO_2 catalyst (Table 1).

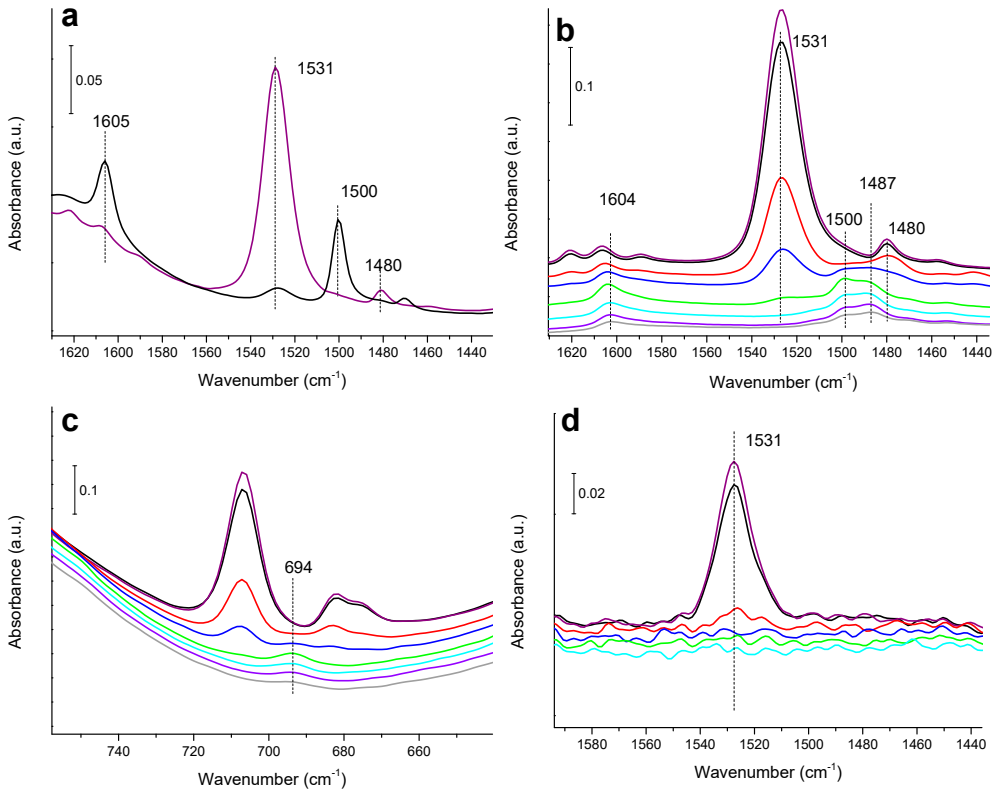

Figure 2. IR spectra of nitrobenzene and H_2 co-adsorbed on: (**a**) Pd/SiO_2, (**b**) Ni/SiO_2 and (**c**) Ni/SiO_2 in the low frequency range, (**d**) Cu/SiO_2 and their reactivity at increasing reaction temperature: 25 °C (black), 60 °C (red), 90 °C (blue), 120 °C (green), 140 °C (cyan), 180 °C (violet) and 200 °C (grey). Purple colored line corresponds to the sample after nitrobenzene and before H_2 co-adsorption at 25 °C.

In the second part of our study, bimetallic catalysts are considered in an attempt to promote the reactivity of the copper-based catalyst. As such, bimetallic $CuNi/SiO_2$ and $CuPd/SiO_2$ systems are studied.

3.3. Synthesis and Characterization of Bimetallic CuNi and CuPd Catalysts

The bimetallic samples have been labelled as CuXMe (Me = Pd or Ni), where X represents the weight percent of the second element (see Table 2). Based on the low metal loading of the second element, only diffraction peaks corresponding to CuO (JCPDS: 48-1548) are observed in the XRD pattern of the calcined $Cu_{0.5}Pd/SiO_2$ and Cu_2Pd/SiO_2 (Figure S5a). However, in the Cu_2Ni/SiO_2 sample, in addition to the diffraction peaks corresponding to CuO, diffraction peaks corresponding to NiO (JCPDS: 78-643) are also observed as a minoritary phase. In the reduced samples, diffraction peaks corresponding to Cu^0 (JCPDS: 4-836) are observed in all samples (Figure S5b). The average copper particle sizes in the reduced $Cu_{0.5}Pd/SiO_2$, Cu_2Pd/SiO_2 and Cu_2Ni/SiO_2 samples, determined according to the Scherrer equation, are ~15 nm in the samples with Pd, and ~30 nm in the Ni sample, similar to that of the monometallic Cu/SiO_2 catalyst (Table 2).

The interaction between both metals can be envisaged by a higher reducibility of the bimetallic catalysts compared to the reference monometallic Cu/SiO_2 catalysts, as visualized from the TPR-H_2 pattern (Figure S6). The surface distribution of both metals in the bimetallic samples has been studied by X-ray photoelectron spectroscopy (XPS) and Infrared spectroscopy (IR) using CO as a probe molecule. The XPS data of the $Cu_{0.5}Pd/SiO_2$, Cu_2Pd/SiO_2 samples (Table S1) show, in both cases, the same Pd/Cu atomic ratio (0.2), whereas, IR of CO, which is more surface sensitive, shows a Pd rich surface in the Cu_2Pd/SiO_2 sample; a Cu rich surface is observed in the $Cu_{0.5}Pd/SiO_2$

sample (Figure S7). In the Cu_2Ni/SiO_2, while the surface composition determined from XPS analysis is higher than in the previous samples (Ni/Cu atomic ratio = 0.9), the IR-CO shows IR peaks predominantly associated with Cu. Here, XPS has a penetration depth of around 6 nm, while IR-CO is sensitive to the upper layer exclusively. On the other hand, while H_2 activation is important for hydrogenation activity, H_2D_2 isotopic studies have been conducted, revealing, in all bimetallic samples, a markedly higher H_2 activation than in the monometallic Cu/SiO_2 one. In fact, the HD formation increases in the order Cu/SiO_2 << $Cu_{0.5}Pd/SiO_2$ < Cu_2Ni/SiO_2 < Cu_2Pd/SiO_2 (Tables 1 and 2).

Table 2. Physico-chemical properties of bimetallic catalysts.

Sample	ICP Cu (%)	ICP Me(%)	H_2 [a] mmol/g	nm [b]	HD/H_2 [c]
$Cu_{0.5}Pd/SiO_2$	26.0	0.5	4.96	15.9	1.18×10^{-1}
Cu_2Pd/SiO_2	23.7	1.6	5.11	14.8	4.44×10^{-1}
Cu_2Ni/SiO_2	25.9	2.0	5.23	34.4	2.89×10^{-1}

[a] H_2 consumptions in the TPR experiments undertaken until 400 °C. [b] Metal particle size determined by the XRD pattern of the reduced samples. [c] HD (mA) in the H_2D_2 isotopic exchange studies relative to the H_2 (mA) in the feed.

3.4. IR Study of Nitrobenzene Hydrogenation on Bimetallic CuNi and CuPd Catalysts

The adsorption of nitrobenzene on the $Cu_{0.5}Pd/SiO_2$, Cu_2Pd/SiO_2 and Cu_2Ni/SiO_2 catalysts, and their evolution at increasing temperatures, is shown in Figure 3.

In particular, in the $Cu_{0.5}Pd/SiO_2$ catalyst, the interaction of nitrobenzene with the catalyst surface is low, analogous to that of the monometallic Cu/SiO_2 catalyst, desorbing when increasing the reaction temperature from 60 to 180 °C (Figure 3a). In fact, IR-CO reveal a small amount of Pd on the catalyst's upper surface, as the surface is enriched with Cu. When increasing the Pd loading in the catalyst (Cu_2Pd/SiO_2), a higher reactivity of nitrobenzene on the catalyst surface is observed, consistent with the Pd enrichment on the upper surface detected by IR-CO. As displayed in Figure 3b, nitrobenzene adsorption leads to the formation of nitrosobenzene (IR band at 1485 cm^{-1}) at 60 °C, achieving a maxima peak intensity at 120 °C, in parallel with the consumption of nitrobenzene. A further increase in the temperature up to 140 and 180 °C results in the disappearance of the band associated with nitrosobenzene and the appearance of new IR bands at 642 and 2199 cm^{-1} (Figure 3b,c), which may be ascribed to Pd–O and/or Pd–N interaction [54]. These bands may arise from a second N–O cleavage of nitrosobenzene, in agreement with the mechanism reported in the DFT studies (see next section). Notoriously, despite the fact that the surface is enriched in Pd, which is a noble metal, the reaction mechanism follows a different path. Thus, a N–O dissociative reaction path, as in the case of non-noble metal catalysts, is observed, in contrast to the NO_2-hydrogenation path observed in noble metals. Next, after co-addition of H_2 at 25 °C and an increase in temperature to 200 °C, the previously reported IR bands at 642 and 2199 cm^{-1} are hydrogenated (not shown).

In the presence of Ni, the behavior of the Cu_2Ni/SiO_2 catalyst is different from the Cu_2Pd/SiO_2, but similar to that of Cu/SiO_2 (Figure 3d), on which nitrobenzene desorption is favored. This is not surprising, based on the low surface distribution of Ni species as detected by IR-CO.

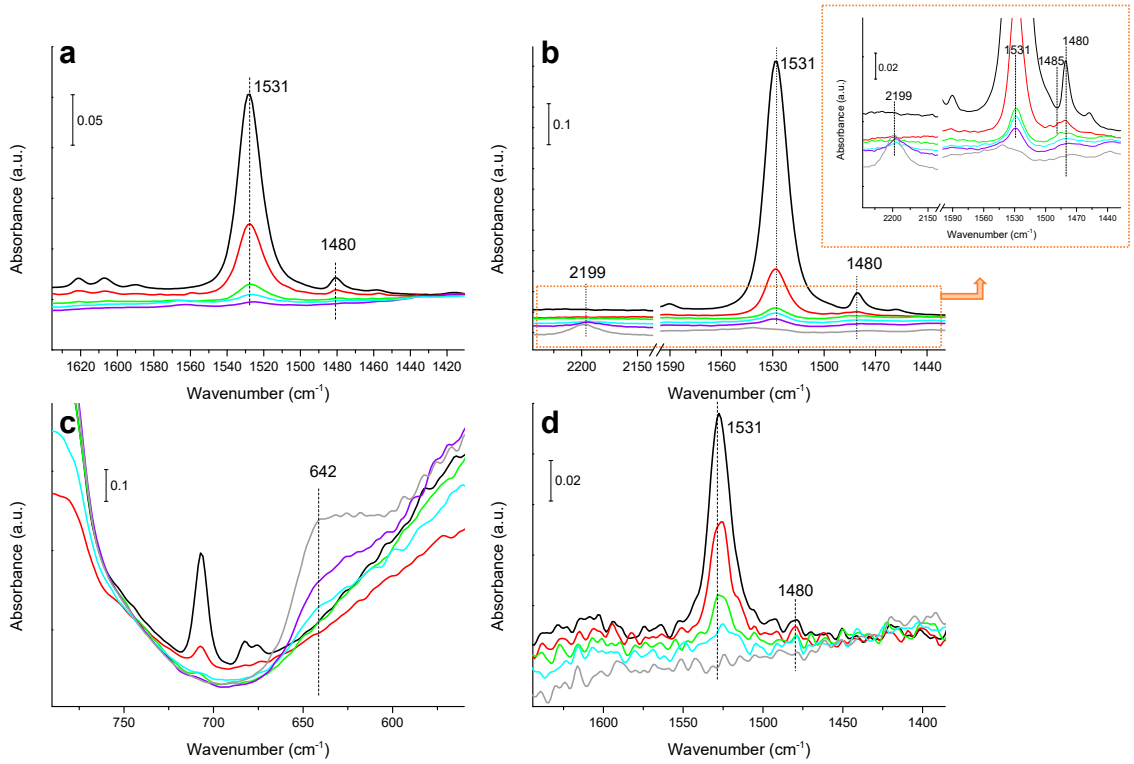

Figure 3. IR spectra of nitrobenzene adsorbed on: (**a**) $Cu_{0.5}Pd/SiO_2$, (**b**) Cu_2Pd/SiO_2 (in the inset a zoom of the bottom part of the IR spectra), (**c**) Cu_2Pd/SiO_2 in the low frequency region, (**d**) Cu_2Ni/SiO_2 and their evolution at increasing temperatures: 25 °C (black), 60 °C (red), 120 °C (green), 140 °C (cyan), 180 °C (violet) and 200 °C (grey).

Finally, the hydrogenation of nitrobenzene in the presence of nitrobenzene and H_2 has been studied by IR on the most active Cu_2Pd/SiO_2 catalyst (Figure 4), displaying a high reactivity toward aniline formation. Thus at 60 °C, aniline and nitrosobenzene are observed, with nitrosobenzene being completely hydrogenated to aniline at 140 °C, with practically 100% selectivity to aniline at this temperature. The reactivity of this sample is lower than that of the pure Pd/SiO_2 catalyst and, as in that case, no intermediate species, such as hydroxylamine, are observed.

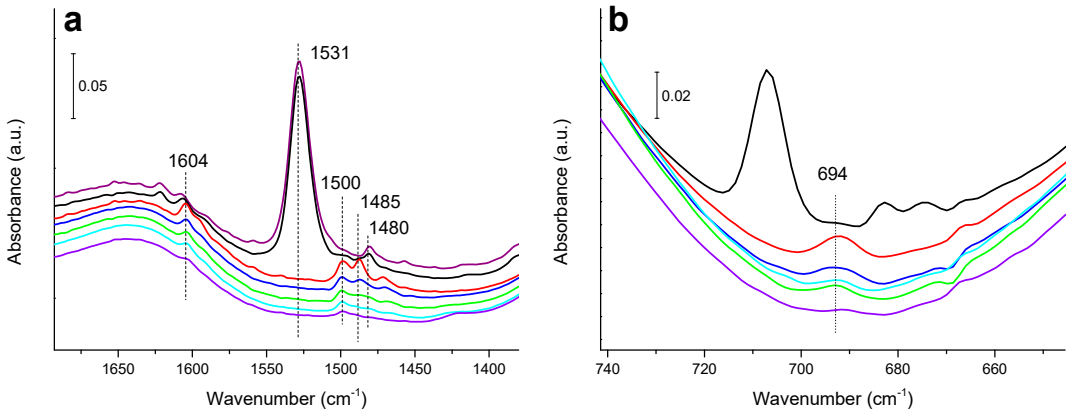

Figure 4. IR study of nitrobenzene and H_2 on: (**a**) Cu_2Pd/SiO_2 sample, and their evolution with the reaction temperature 25 °C (black), 60 °C (red), 90 °C (blue), 120 °C (green), 140 °C (cyan) and 180 °C (violet). Purple colored line corresponds to the sample after nitrobenzene and before H_2 co-adsorption at 25 °C. (**b**) corresponding IR spectra in the low frequency range.

3.5. DFT Study of Nitrobenzene Adsorption and Reaction on Mono- and Bimetallic Catalysts

As described in previous studies [41,42], the main elementary steps in the mechanism of nitrobenzene hydrogenation to aniline catalyzed by non-noble metals are those summarized in Equations (8)–(13):

$$H_2 \rightarrow 2H^* \quad (8)$$

$$Ph\text{-}NO_2 \rightarrow Ph\text{-}NO_2^* \quad (9)$$

$$Ph\text{-}NO_2^* \rightarrow Ph\text{-}NO^* + O^* \quad (10)$$

$$Ph\text{-}NO^* \rightarrow Ph\text{-}N^* + O^* \quad (11)$$

$$Ph\text{-}N^* + H^* \rightarrow Ph\text{-}NH^* \quad (12)$$

$$Ph\text{-}NH^* + H^* \rightarrow Ph\text{-}NH_2^* \quad (13)$$

H_2 dissociation into two adsorbed H atoms, according to (8), involves low or null activation barriers on Ni(111) and Pd(111), but it is more difficult on a Cu(111) surface because H_2 does not adsorb on the metal but reacts from the gas phase with a calculated activation energy of 8.5 kcal/mol. [42] However, the addition of just a single Ni atom on a perfect Cu(111) surface, as in the $Ni_1Cu(111)$ slab model depicted in Figure 5, is enough to bind H_2 with a calculated adsorption energy of −9.3 kcal/mol and dissociate it with a slightly lower barrier of 7.8 kcal/mol. Then, after nitrobenzene adsorption on the metal surface according to Equation (9), one of the two NO bonds of the nitro group is easily broken, generating nitrosobenzene and one surface oxygen atom, (see Equation (10)). The subsequent dissociation of the NO bond in nitrosobenzene, Equation (11), yields a highly stable Ph–N* intermediate with one N atom tri-coordinated to the surface metal atoms. The activation energies for these two NO bond breaking steps, summarized in Table 3, are similar in the three models considered, and always equal or lower than 10 kcal/mol. However, the interaction between the adsorbed species and the metal surface is clearly stronger in the case of Ni(111), as indicated by the more exothermic reaction energy values listed in Table 3 and the energy profiles compared in Figure 5. Interestingly, the stability of the Ph–N* intermediate is modified by the presence of just one Ni atom on the Cu(111) surface, and the calculated reaction energy for step (11) decreases by 8 kcal/mol in $Ni_1Cu/(111)$ compared with Cu(111). The lower stability of Ph–N* intermediate facilitates its subsequent hydrogenation according to (12) and (13) to finally yield adsorbed aniline. While these results would suggest a better catalytic performance of the bimetallic Cu_2Ni/SiO_2 catalyst when compared to Cu/SiO_2, the IR study described above shows that neither Cu/SiO_2 nor Cu_2Ni/SiO_2 are able to activate nitrobenzene, which desorbs when temperature is raised to 200 °C. The same behavior is observed with the $Cu_{0.5}Pd/SiO_2$ sample containing a low amount of Pd on the catalyst surface, but not with the Cu_2Pd/SiO_2 sample, in which small surface Pd regions are detected by IR-CO.

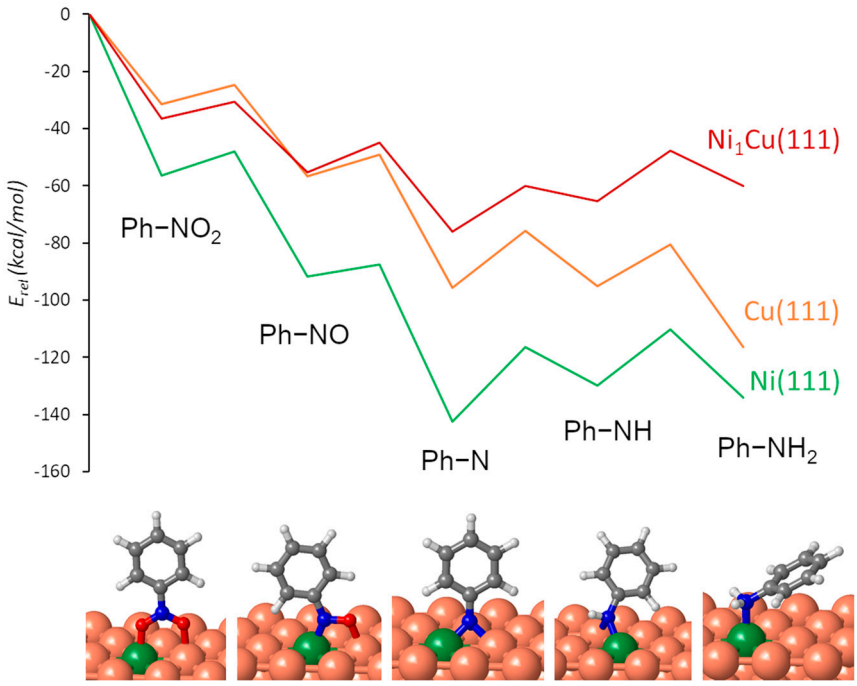

Figure 5. Calculated energy profiles for nitrobenzene hydrogenation to aniline on Ni(111), Cu(111) and $Ni_1Cu(111)$ surfaces, and optimized structures of the stable minima on the bimetallic catalyst model. Cu, Ni, C, N, O and H atoms are depicted as orange, green, gray, blue, red and white balls, respectively.

Table 3. Calculated activation (E_{act}) and reaction (ΔE) energies in kcal/mol for nitrobenzene hydrogenation on mono- and bimetallic non-noble metal catalysts.

		Ni(111)		Cu(111)		$Ni_1Cu(111)$	
		E_{act}	ΔE	E_{act}	ΔE	E_{act}	ΔE
(10)	Ph–NO_2* → Ph–NO* + O*	8.3	−35.6	6.9	−25.2	5.8	−24.7
(11)	Ph–NO* → Ph–N* + O*	4.3	−50.2	7.5	−39.1	10.3	−31.1
(12)	Ph–N* + H* → Ph–NH*	26.1	12.4	19.8	0.8	15.9	−5.1
(13)	Ph–NH* + H* → Ph–NH_2*	19.6	−4.1	14.3	−21.4	17.6	−12.5

At this point, it becomes necessary to study the adsorption of nitrobenzene and its evolution with temperature on catalyst models able to accurately represent the surface composition of the mono- and bimetallic samples experimentally tested. To this end, the Gibbs free energies of nitrobenzene adsorption were calculated at increasing temperatures for Cu(111), Ni_1Cu/(111), Pd(111), and a series of $Pd_nCu(111)$ slab models were generated by replacing an increasing amount of Cu atoms with Pd_n, n = 1 to n = 10 (see Figures 6 and 7). As previously reported [42], nitrobenzene adsorbs normally to the Cu(111) surface with each O atom of the nitro group directly bonded to one surface Cu atom. In contrast, nitrobenzene adsorbs parallel to the Pd(111) surface, with the C atoms of the aromatic ring strongly bonded to the surface Pd atoms, and with the nitro group tilted with only one O atom interacting with the metal. The most stable structure for nitrobenzene adsorption on $Pd_1Cu(111)$ is similar to that found for Ni_1Cu/(111), i.e., normal to the surface and with one of the O atoms of the nitro group directly bonded to the isolated Ni or Pd atom. Introduction of Pd atoms in the top layer of the catalyst, as in $Pd_5Cu(111)$ model (see Figure 6), displaces adsorbed nitrobenzene in such a way that the two O atoms of the nitro group are directly bonded to two Cu atoms, but the molecule is partly bent due to some interaction between the aromatic ring and the surface Pd atoms. The arrangement of the

Pd atoms in $Pd_6Cu(111)$, $Pd_8Cu(111)$ and $Pd_{10}Cu(111)$ models, occupying positions in the two uppermost layers of the model, enhances the interaction through the aromatic ring and results in de-coordination of the nitro group from the catalyst surface, with adsorption geometries quite similar to that found on pure Pd(111) surface. These geometrical changes are clearly reflected in the calculated Gibbs free adsorption energies plotted in Figure 7. Nitrobenzene interaction with Cu(111) is weak, and desorption could be spontaneous when raising the temperature. The addition of isolated Ni or Pd atoms slightly modifies this interaction, enhancing it in the first case (dotted orange line in Figure 7) and weakening it in the second one (yellow dotted line in Figure 7). In agreement with this trend, the normal adsorption of nitrobenzene on Ni(111) is more stable than on Cu(111) and on $Ni_1Cu/(111)$, despite the equivalent geometry. The destabilizing effect associated with Pd is reversed as the number of Pd atoms increases and the nature of the interaction changes. Thus, the Gibbs free energy of adsorption on $Pd_5Cu(111)$ model (red dotted line) is equivalent to that on Cu(111) but, when the interaction through the aromatic ring becomes predominant, the system is significantly stabilized, and no spontaneous desorption is expected in the range of considered temperatures (purple and blue dotted lines in Figure 7).

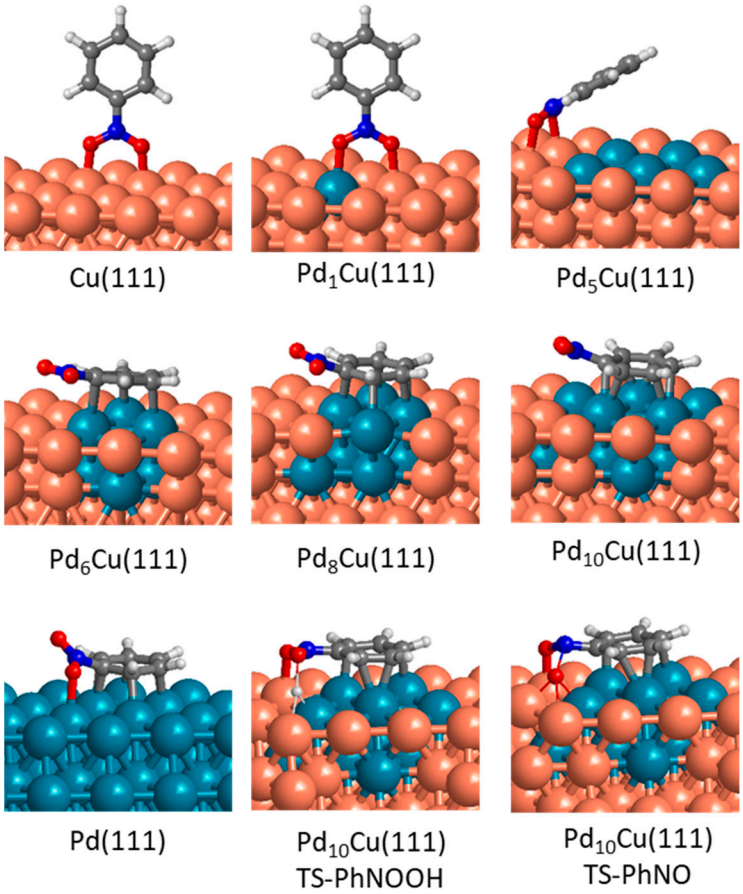

Figure 6. Optimized structures of nitrobenzene adsorbed on mono- and bimetallic catalyst models, and of the transition states for the first hydrogen transfer (TSA) and the first NO bond-breaking (TSB) steps of the mechanism on the $Pd_{10}Cu(111)$ model. Cu, Pd, C, N, O and H atoms are depicted as orange, cyan, gray, blue, red and white balls, respectively.

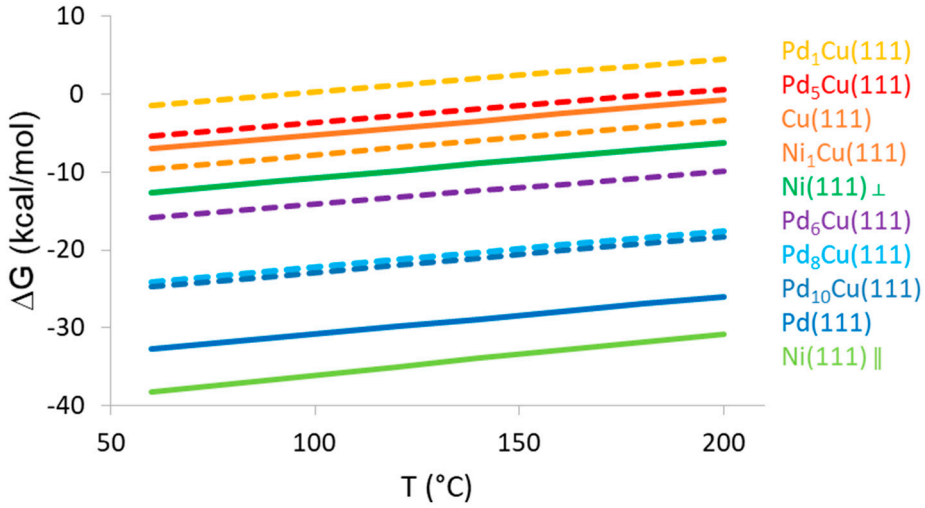

Figure 7. Gibbs free energies of adsorption on nitrobenzene on mono- and bimetallic catalyst models as a function of temperature.

These data are fully consistent with the experimental results found for mono-metallic Cu/SiO_2, Ni/SiO_2 and Pd/SiO_2 catalysts. The two non-noble metal based catalysts should be able to activate the nitro group in the absence of H_2, but the weak adsorption of nitrobenzene on Cu(111) leads to its spontaneous desorption before bond-breaking occurs. The higher stability of nitrobenzene adsorbed on Ni(111) makes possible the subsequent reaction following the proposed pathway via NO bond dissociation, and nitrosobenzene is observed by IR spectroscopy at 60 °C. After the addition of H_2, it is necessary to raise the temperature to 90 °C to detect aniline, in agreement with the higher activation barriers calculated for the hydrogen transfer steps (see Table 3). In contrast, Pd behaves as a noble metal and is not able to dissociate the NO bond in the absence of H_2. However, aniline is already detected at 25 °C when the experiments are carried out in the presence of both nitrobenzene and H_2, confirming the different mechanism operating on Pd/SiO_2 catalysts.

The experimental results obtained with the bimetallic catalysts are also explained by the theoretical data. Too dispersed Ni or Pd species on the Cu(111) surface do not sufficiently stabilize adsorbed nitrobenzene, and therefore the behavior of Cu_2Ni/SiO_2 and $Cu_{0.5}Pd/SiO_2$ samples is similar to that of Cu/SiO_2. However, the small agglomerates of Pd atoms formed on the surface of the Cu_2Pd/SiO_2 sample are able to bind nitrobenzene and make it react, both in absence and presence of H_2. Indeed, the two pathways described in Scheme 1b for noble and non-noble metals are accessible in this system. Starting from nitrobenzene adsorbed on the $Pd_{10}Cu(111)$ model, we calculated the transition states for both NO dissociation to give nitrosobenzene (TS-PhNO in Figure 6) and for H transfer to form adsorbed Ph–NOOH (TS-PhNOOH in Figure 6). The calculated activation energies listed in Table 4 indicate that H transfer is preferred in this bimetallic system with a barrier of 9 kcal/mol, but formation of nitrosobenzene with a calculated barrier of 19.3 kcal/mol is also energetically accessible. Notice that the calculated E_{act} values for the hydrogen transfer steps to Ph–N* and Ph–NH* intermediates on Ni(111) are larger (26.1 and 19.6 kcal/mol, see Table 4), and the E_{act} value for the first hydrogenation step to form Ph-NOOH* on Pd(111) is quite close, 15.9 kcal/mol (see Table 4). These values are in excellent agreement with the observation of nitrosobenzene on the Cu_2Pd/SiO_2 sample, both in the absence and presence of H_2 and with the fast formation of aniline in the presence of H_2.

Table 4. Activation energies in kcal/mol for the first elementary step of each of the two pathways considered for nitrobenzene hydrogenation on different mono- and bimetallic catalyst models.

	Ni(111) [a]	Cu(111) [a]	Pd(111) [a]	$Pd_{10}Cu(111)$
Ph-NO_2* + H* → Ph-NOOH*	25.5	12.9	15.9	9.0
Ph-NO_2* → Ph-NO* + O*	8.3	6.9	29.4	19.3

[a] Values from ref. [42].

4. Conclusions

Based on previous theoretical studies proposing that nitrobenzene hydrogenation on noble and non-noble metals follows different pathways, in this work, mono- and bimetallic catalysts based on Ni, Cu and Pd have been synthesized, characterized and their interaction with nitrobenzene and H_2 has been investigated by IR spectroscopy and DFT calculations. First, it has been confirmed by IR spectroscopy that nitrobenzene is directly converted into nitrosobenzene on large Ni particles supported on SiO_2, and that the addition or co-adsorption of H_2 results in the formation of aniline, following the mechanism proposed theoretically in ref. [41]. In contrast, neither Cu nor Pd are able to activate nitrobenzene in the absence of H_2. Co-adsorption of nitrobenzene and H_2 on Pd/SiO_2 leads to aniline without detection of nitosobenzene, in agreement with the pathway proposed for noble metals, while Cu/SiO_2 is not active due to its inability to dissociate H_2 [42], as confirmed by H_2D_2 isotopic studies. Second, with the aim of improving the H_2 dissociation ability of Cu/SiO_2, bimetallic catalysts based on Cu doped with different amounts of either Ni or Pd were prepared, characterized by XPS and IR of CO adsorption and their interaction with nitrobenzene was followed by IR spectroscopy. When the amount of doping metal on the surface of the Cu nanoparticles is low, the bimetallic catalysts behave as Cu/SiO_2, irrespective of the nature of the doping metal, either Ni or Pd. However, the bimetallic Cu_2Pd/SiO_2 catalyst containing a Pd-enriched surface exhibits not only enhanced H_2 activation but also different reactivity. Thus, interaction of Cu_2Pd/SiO_2 with nitrobenzene alone results in the formation of nitrosobenzene according to the N–O dissociation mechanism proposed for non-noble metals, while co-adsorption of H_2 and nitrobenzene leads to fast hydrogenation following the H-transfer pathway preferred on noble metals.

Supplementary Materials: The following are available online at https://www.mdpi.com/article/10.3390/nano11082037/s1, Figure S1. XRD pattern of the calcined (a) and (b) reduced monometallic Ni/SiO_2, Cu/SiO_2 and Pd/SiO_2 catalysts, Figure S2: IR spectra of nitrobenzene adsorption at saturation coverage on Cu/SiO_2 (blue), Pd/SiO_2 (red), Ni/SiO_2 (green). Spectra normalized to sample weight. The lower intensity of the IR signal in the Cu/SiO_2 and Pd/SiO_2 samples agrees with the low interaction of nitrobenzene on both metals, Figure S3: IR spectra of nitrosobenzene formed on the Ni/SiO_2 catalyst and after co-addition of H_2 at 25 °C (red line). Then, the temperature is increased to 90 °C (blue), 120 °C (green), 160 °C (magenta) and 200 °C (grey). Aniline formation (IR band at 1605, 1500 and 694 cm^{-1}) is detected at 200 °C, IR spectra of nitrobenzene and H_2 co-adsorbed on Ni/SiO_2, and their reactivity at increasing reaction temperature: 25 °C (black), 60 °C (red), 90 °C (blue), 120 °C (green), 140 °C (cyan), 180 °C (violet), 200 °C (grey). In violet bold after cooling down the sample from 180 °C to 25 °C allowing re-adsorption of the gas phase, Figure S5: XRD pattern of the calcined (a) and (b) reduced bimetallic Cu_2Pd/SiO_2, $Cu_{0.5}Pd/SiO_2$ and Cu_2Ni/SiO_2 catalysts, TPR-H2 of monometallic Cu/SiO_2 and bimetallic Cu_2Pd/SiO_2, $Cu_{0.5}Pd/SiO_2$ and Cu_2Ni/SiO_2 catalysts. The addition of Pd or Ni to the Cu monometallic catalyst, favour H_2 activation (as determined from the H_2D_2 isotopic exchange experiments), resulting in a higher catalyst reducibility, IR spectra of CO adsorption at −170 °C on (a) $Cu_{0.5}Pd/SiO_2$, (b) Cu_2Pd/SiO_2, (c) Cu_2Ni/SiO_2, Table S1. Surface composition determined by XPS.

Author Contributions: Conceptualization, P.C. and M.B.; Methodology, P.C., R.M. and M.B.; Formal Analysis, P.C., R.M., C.C.M., M.D.S. and M.B.; Investigation, P.C., R.M. and M.B.; Resources, P.C. and M.B.; Writing—Original Draft, R.M., M.B. and P.C.; Writing—Review and Editing, M.B., C.C.M., M.D.S., R.M. and P.C.; Visualization, M.B. and P.C.; Supervision, P.C. and M.B.; Funding Acquisition, P.C. and M.B. All authors have read and agreed to the published version of the manuscript.

Funding: This research was funded by Spanish Government through "Severo Ochoa" program (SEV-2016-0683, MINECO), MAT2017-82288-C2-1-P (AEI/FEDER, UE), RTI2018-099668-B-C21 (MINECO) and by Generalitat Valenciana through AICO/2017/153 Project.

Acknowledgments: Computations were performed on the Tirant III cluster of the Servei d'Informàtica of the University of Valencia (SIUV). Red Española de Supercomputación (RES) and SIUV are gratefully acknowledged for computational resources and technical support. R.M. acknowledges "La Caixa—Severo Ochoa" International PhD Fellowships (call 2015).

Conflicts of Interest: The authors declare no conflict of interest.

References

1. Tafesh, A.M.; Weiguny, J. A Review of the Selective Catalytic Reduction of Aromatic Nitro Compounds into Aromatic Amines, Isocyanates, Carbamates, and Ureas Using CO. *Chem. Rev.* **1996**, *96*, 2035–2052. [CrossRef] [PubMed]
2. Sheldon, R.A.; van Bekkum, H. *Fine Chemicals through Heterogeneous Catalysis*; John Wiley & Sons: Hoboken, NJ, USA, 2008; ISBN 3527612971.
3. Blaser, H.-U.; Malan, C.; Pugin, B.; Spindler, F.; Steiner, H.; Studer, M. Selective Hydrogenation for Fine Chemicals: Recent Trends and New Developments. *Adv. Synth. Catal.* **2003**, *345*, 103–151. [CrossRef]
4. Blaser, H.-U.; Steiner, H.; Studer, M. Selective Catalytic Hydrogenation of Functionalized Nitroarenes: An Update. *ChemCatChem* **2009**, *1*, 210–221. [CrossRef]
5. Boymans, E.; Boland, S.; Witte, P.T.; Müller, C.; Vogt, D. Chemoselective Hydrogenation of Functionalized Nitroarenes Using Supported Mo Promoted Pt Nanoparticles. *ChemCatChem* **2013**, *5*, 431–434. [CrossRef]
6. Lara, P.; Philippot, K. The Hydrogenation of Nitroarenes Mediated by Platinum Nanoparticles: An Overview. *Catal. Sci. Technol.* **2014**, *4*, 2445–2465. [CrossRef]
7. Pietrowski, M. Recent Developments in Heterogeneous Selective Hydrogenation of Halogenated Nitroaromatic Compounds to Halogenated Anilines. *Curr. Org. Synth.* **2012**, *9*, 470–487. [CrossRef]
8. Formenti, D.; Ferretti, F.; Scharnagl, F.K.; Beller, M. Reduction of Nitro Compounds Using 3d-Non-Noble Metal Catalysts. *Chem. Rev.* **2019**, *119*, 2611–2680. [CrossRef]
9. Corma, A.; Serna, P. Chemoselective Hydrogenation of Nitro Compounds with Supported Gold Catalysts. *Science* **2006**, *313*, 332. [CrossRef]
10. Serna, P.; Concepción, P.; Corma, A. Design of Highly Active and Chemoselective Bimetallic Gold–Platinum Hydrogenation Catalysts through Kinetic and Isotopic Studies. *J. Catal.* **2009**, *265*, 19–25. [CrossRef]
11. Wei, H.; Liu, X.; Wang, A.; Zhang, L.; Qiao, B.; Yang, X.; Huang, Y.; Miao, S.; Liu, J.; Zhang, T. FeO_x-Supported Platinum Single-Atom and Pseudo-Single-Atom Catalysts for Chemoselective Hydrogenation of Functionalized Nitroarenes. *Nat. Commun.* **2014**, *5*, 5634. [CrossRef]
12. Shimizu, K.; Miyamoto, Y.; Satsuma, A. Size- and Support-Dependent Silver Cluster Catalysis for Chemoselective Hydrogenation of Nitroaromatics. *J. Catal.* **2010**, *270*, 86–94. [CrossRef]
13. Lin, L.; Yao, S.; Gao, R.; Liang, X.; Yu, Q.; Deng, Y.; Liu, J.; Peng, M.; Jiang, Z.; Li, S.; et al. A Highly CO-Tolerant Atomically Dispersed Pt Catalyst for Chemoselective Hydrogenation. *Nat. Nanotechnol.* **2019**, *14*, 354–361. [CrossRef] [PubMed]
14. Corma, A.; Serna, P.; Concepción, P.; Calvino, J.J. Transforming Nonselective into Chemoselective Metal Catalysts for the Hydrogenation of Substituted Nitroaromatics. *J. Am. Chem. Soc.* **2008**, *130*, 8748–8753. [CrossRef]
15. Macino, M.; Barnes, A.J.; Althahban, S.M.; Qu, R.; Gibson, E.K.; Morgan, D.J.; Freakley, S.J.; Dimitratos, N.; Kiely, C.J.; Gao, X.; et al. Tuning of Catalytic Sites in Pt/TiO_2 Catalysts for the Chemoselective Hydrogenation of 3-Nitrostyrene. *Nat. Catal.* **2019**, *2*, 873–881. [CrossRef]
16. Wang, Y.; Qin, R.; Wang, Y.; Ren, J.; Zhou, W.; Li, L.; Ming, J.; Zhang, W.; Fu, G.; Zheng, N. Chemoselective Hydrogenation of Nitroaromatics at the Nanoscale Iron(III)–OH–Platinum Interface. *Angew. Chem. Int. Ed.* **2020**, *59*, 12736–12740. [CrossRef]
17. Vilé, G.; Almora-Barrios, N.; López, N.; Pérez-Ramírez, J. Structure and Reactivity of Supported Hybrid Platinum Nanoparticles for the Flow Hydrogenation of Functionalized Nitroaromatics. *ACS Catal.* **2015**, *5*, 3767–3778. [CrossRef]
18. Takasaki, M.; Motoyama, Y.; Higashi, K.; Yoon, S.-H.; Mochida, I.; Nagashima, H. Chemoselective Hydrogenation of Nitroarenes with Carbon Nanofiber-Supported Platinum and Palladium Nanoparticles. *Org. Lett.* **2008**, *10*, 1601–1604. [CrossRef]
19. Boronat, M.; Concepción, P.; Corma, A.; González, S.; Illas, F.; Serna, P. A Molecular Mechanism for the Chemoselective Hydrogenation of Substituted Nitroaromatics with Nanoparticles of Gold on TiO_2 Catalysts: A Cooperative Effect between Gold and the Support. *J. Am. Chem. Soc.* **2007**, *129*, 16230–16237. [CrossRef]
20. Boronat, M.; Corma, A. Origin of the Different Activity and Selectivity toward Hydrogenation of Single Metal Au and Pt on TiO_2 and Bimetallic $Au-Pt/TiO_2$ Catalysts. *Langmuir* **2010**, *26*, 16607–16614. [CrossRef]
21. Boronat, M.; Concepción, P. Combined Theoretical and Spectroscopic Mechanistic Studies for Improving Activity and Selectivity in Heterogeneous Catalysis. *Catal. Today* **2017**, *285*, 166–178. [CrossRef]
22. Westerhaus, F.A.; Jagadeesh, R.V.; Wienhöfer, G.; Pohl, M.-M.; Radnik, J.; Surkus, A.-E.; Rabeah, J.; Junge, K.; Junge, H.; Nielsen, M.; et al. Heterogenized Cobalt Oxide Catalysts for Nitroarene Reduction by Pyrolysis of Molecularly Defined Complexes. *Nat. Chem.* **2013**, *5*, 537–543. [CrossRef] [PubMed]

23. Jagadeesh, R.V.; Surkus, A.-E.; Junge, H.; Pohl, M.-M.; Radnik, J.; Rabeah, J.; Huan, H.; Schünemann, V.; Brückner, A.; Beller, M. Nanoscale Fe_2O_3-Based Catalysts for Selective Hydrogenation of Nitroarenes to Anilines. *Science* **2013**, *342*, 1073. [CrossRef]
24. Wei, Z.; Wang, J.; Mao, S.; Su, D.; Jin, H.; Wang, Y.; Xu, F.; Li, H.; Wang, Y. In Situ-Generated Co_0-Co_3O_4/N-Doped Carbon Nanotubes Hybrids as Efficient and Chemoselective Catalysts for Hydrogenation of Nitroarenes. *ACS Catal.* **2015**, *5*, 4783–4789. [CrossRef]
25. Liu, L.; Concepción, P.; Corma, A. Non-Noble Metal Catalysts for Hydrogenation: A Facile Method for Preparing Co Nanoparticles Covered with Thin Layered Carbon. *J. Catal.* **2016**, *340*, 1–9. [CrossRef]
26. Ren, Y.; Wei, H.; Yin, G.; Zhang, L.; Wang, A.; Zhang, T. Oxygen Surface Groups of Activated Carbon Steer the Chemoselective Hydrogenation of Substituted Nitroarenes over Nickel Nanoparticles. *Chem. Commun.* **2017**, *53*, 1969–1972. [CrossRef]
27. Sun, X.; Olivos-Suarez, A.I.; Osadchii, D.; Romero, M.J.V.; Kapteijn, F.; Gascon, J. Single Cobalt Sites in Mesoporous N-Doped Carbon Matrix for Selective Catalytic Hydrogenation of Nitroarenes. *J. Catal.* **2018**, *357*, 20–28. [CrossRef]
28. Yang, F.; Wang, M.; Liu, W.; Yang, B.; Wang, Y.; Luo, J.; Tang, Y.; Hou, L.; Li, Y.; Li, Z.; et al. Atomically Dispersed Ni as the Active Site towards Selective Hydrogenation of Nitroarenes. *Green Chem.* **2019**, *21*, 704–711. [CrossRef]
29. Pan, H.; Peng, Y.; Lu, X.; He, J.; He, L.; Wang, C.; Yue, F.; Zhang, H.; Zhou, D.; Xia, Q. Well-Constructed Ni@CN Material Derived from Di-Ligands Ni-MOF to Catalyze Mild Hydrogenation of Nitroarenes. *Mol. Catal.* **2020**, *485*, 110838. [CrossRef]
30. Tang, Q.; Yuan, Z.; Jin, S.; Yao, K.; Yang, H.; Chi, Q.; Liu, B. Biomass-Derived Carbon-Supported Ni Catalyst: An Effective Heterogeneous Non-Noble Metal Catalyst for the Hydrogenation of Nitro Compounds. *React. Chem. Eng.* **2020**, *5*, 58–65. [CrossRef]
31. Petkar, D.R.; Kadu, B.S.; Chikate, R.C. Highly Efficient and Chemoselective Transfer Hydrogenation of Nitroarenes at Room Temperature over Magnetically Separable Fe–Ni Bimetallic Nanoparticles. *RSC Adv.* **2014**, *4*, 8004–8010. [CrossRef]
32. Zhang, J.; Lu, G.; Cai, C. Chemoselective Transfer Hydrogenation of Nitroarenes by Highly Dispersed Ni-Co BMNPs. *Catal. Commun.* **2016**, *84*, 25–29. [CrossRef]
33. Liu, L.; Gao, F.; Concepción, P.; Corma, A. A New Strategy to Transform Mono and Bimetallic Non-Noble Metal Nanoparticles into Highly Active and Chemoselective Hydrogenation Catalysts. *J. Catal.* **2017**, *350*, 218–225. [CrossRef]
34. Yu, H.; Tang, W.; Li, K.; Yin, H.; Zhao, S.; Zhou, S. Design of Cu-Based Intermetallic Nanocrystals for Enhancing Hydrogenation Selectivity. *Chem. Eng. Sci.* **2019**, *196*, 402–413. [CrossRef]
35. Huang, L.; Lv, Y.; Wu, S.; Liu, P.; Xiong, W.; Hao, F.; Luo, H. Activated Carbon Supported Bimetallic Catalysts with Combined Catalytic Effects for Aromatic Nitro Compounds Hydrogenation under Mild Conditions. *Appl. Catal. A Gen.* **2019**, *577*, 76–85. [CrossRef]
36. González-Vera, D.; Bustamante, T.M.; de León, J.N.D.; Dinamarca, R.; Morales, R.; Osorio-Vargas, P.A.; Torres, C.C.; Campos, C.H. Chemoselective Nitroarene Hydrogenation over Ni-Pd Alloy Supported on TiO_2 Prepared from Ilmenite-Type $PdxNi1-xTiO_3$. *Mater. Today Commun.* **2020**, *24*, 101091. [CrossRef]
37. Haber, F. Gradual Electrolytic Reduction of Nitrobenzene with Limited Cathode Potential. *Elektrochem. Angew. Phys. Chem.* **1898**, *22*, 506–514.
38. Sheng, T.; Qi, Y.-J.; Lin, X.; Hu, P.; Sun, S.-G.; Lin, W.-F. Insights into the Mechanism of Nitrobenzene Reduction to Aniline over Pt Catalyst and the Significance of the Adsorption of Phenyl Group on Kinetics. *Chem. Eng. J.* **2016**, *293*, 337–344. [CrossRef]
39. Zhang, L.; Jiang, J.; Shi, W.; Xia, S.; Ni, Z.; Xiao, X. Insights into the Hydrogenation Mechanism of Nitrobenzene to Aniline on Pd3/Pt(111): A Density Functional Theory Study. *RSC Adv.* **2015**, *5*, 34319–34326. [CrossRef]
40. Mahata, A.; Rai, R.K.; Choudhuri, I.; Singh, S.K.; Pathak, B. Direct vs. Indirect Pathway for Nitrobenzene Reduction Reaction on a Ni Catalyst Surface: A Density Functional Study. *Phys. Chem. Chem. Phys.* **2014**, *16*, 26365–26374. [CrossRef]
41. Millán, R.; Liu, L.; Boronat, M.; Corma, A. A New Molecular Pathway Allows the Chemoselective Reduction of Nitroaromatics on Non-Noble Metal Catalysts. *J. Catal.* **2018**, *364*, 19–30. [CrossRef]
42. Millán, R.; Boronat, M. Hydrogenation of Substituted Nitroaromatics on Non-Noble Metal Catalysts: Mechanistic Insights to Improve Selectivity. *Faraday Discuss.* **2021**, *229*, 297–317. [CrossRef] [PubMed]
43. Kresse, G.; Furthmüller, J. Efficient Iterative Schemes for Ab Initio Total-Energy Calculations Using a Plane-Wave Basis Set. *Phys. Rev. B* **1996**, *54*, 11169–11186. [CrossRef]
44. Perdew, J.P.; Burke, K.; Ernzerhof, M. Fluid Vesicles in Shear Flow. *Phys. Rev. Lett.* **1996**, *77*, 3865–3868. [CrossRef] [PubMed]
45. Perdew, J.P.; Burke, K.; Ernzerhof, M. Generalized Gradient Approximation Made Simple (Vol 77, Pg 3865, 1996). *Phys. Rev. Lett.* **1997**, *78*, 1396. [CrossRef]
46. Grimme, S. Semiempirical GGA-Type Density Functional Constructed with a Long-Range Dispersion Correction. *J. Comput. Chem.* **2006**, *27*, 1787–1799. [CrossRef]
47. Blöchl, P.E.; Jepsen, O.; Andersen, O.K. Improved Tetrahedron Method for Brillouin-Zone Integrations. *Phys. Rev. B* **1994**, *49*, 16223–16233. [CrossRef]
48. Kresse, G.; Joubert, D. From ultrasoft pseudopotentials to the projector augmented-wave method. *Phys. Rev. B Condens. Matter* **1999**, *59*, 1758–1775. [CrossRef]
49. Heyden, A.; Bell, A.T.; Keil, F.J. Efficient Methods for Finding Transition States in Chemical Reactions: Comparison of Improved Dimer Method and Partitioned Rational Function Optimization Method. *J. Chem. Phys.* **2005**, *123*, 224101. [CrossRef]
50. Henkelman, G.; Jónsson, H. A Dimer Method for Finding Saddle Points on High Dimensional Potential Surfaces Using Only First Derivatives. *J. Chem. Phys.* **1999**, *111*, 7010–7022. [CrossRef]

51. Monkhorst, H.J.; Pack, J.D. Special Points for Brillouin-Zone Integrations. *Phys. Rev. B* **1976**, *13*, 5188–5192. [CrossRef]
52. Richner, G.; van Bokhoven, J.A.; Neuhold, Y.-M.; Makosch, M.; Hungerbühler, K. In Situ Infrared Monitoring of the Solid/Liquid Catalyst Interface during the Three-Phase Hydrogenation of Nitrobenzene over Nanosized Au on TiO_2. *Phys. Chem. Chem. Phys.* **2011**, *13*, 12463–12471. [CrossRef] [PubMed]
53. Combita, D.; Concepción, P.; Corma, A. Gold Catalysts for the Synthesis of Aromatic Azocompounds from Nitroaromatics in One Step. *J. Catal.* **2014**, *311*, 339–349. [CrossRef]
54. Baylet, A.; Marécot, P.; Duprez, D.; Castellazzi, P.; Groppi, G.; Forzatti, P. In Situ Raman and in SituXRD Analysis of PdO Reduction and Pd° Oxidation Supported on γ-Al_2O_3 Catalyst under Different Atmospheres. *Phys. Chem. Chem. Phys.* **2011**, *13*, 4607–4613. [CrossRef] [PubMed]